CrossMark

ORIGINAL PAPER

Experimental investigation and design of a shape-variable compressor cascade

J. H. Krone[1] · O. Huxdorf[2] · J. Riemenschneider[2] · H. P. Monner[2] ·
F. Schur[1] · J. Friedrichs[1] · M. Wiedemann[2]

Abstract The design of jet engine compressor blading always implies a compromise between design and off-design operation. The reason for this is a fixed blade geometry which has to be operated over a wide range of operating conditions. Consequently, maximum achievable efficiencies at design operation are limited by off-design requirements, e.g., a certain stall margin. This paper describes an approach using shape-variable blades equipped with integrated piezoceramic-based macro fiber composite (MFC) Actuators on the blade's suction and pressure sides. By applying a voltage to these actuators, it is possible to increase and to decrease the blade stagger angle and therefore the blade turning. Compared to a conventional fixed blade profile, the actuated design is thus adaptable within a certain range regarding ambient conditions. The first part of the paper describes the geometry and structure of the shape-variable blades for use in a compressor cascade experiment. In the next part, the three-dimensional deformation behavior of all manufactured blades at different shape conditions is characterized with a photogrammetric measurement system called ATOS. The first results without aerodynamic loads show an average displacement at the trailing edge of approximately $\Delta z \approx 0.9$ mm compared to the non-actuated condition. This corresponds to an average outlet angle variation of approximately $\Delta \kappa_2 \approx \pm 1°$. The third part of the paper presents the results of the low speed cascade experiment using a fully actuated cascade. On the one hand, the objective is to determine the influence of blade actuation on aerodynamic characteristics such as flow outlet angle, total pressure loss and pressure distributions. On the other hand, optical blade displacement measurements are used to investigate combined 2D- and 3D-deformation effects of blade actuation in conjunction with aerodynamic loads. For these measurements, the ATOS system is also used. The wake evaluations show that maximum blade actuation leads to flow outlet angle deviations up to $\pm 1°$ which can be described by an almost linear shift of the cascade performance without changing the loss distribution significantly. Furthermore, for the chosen profile this margin is approximately constant over the operating range.

List of symbols

Abbreviations
AoA	Angle of attack
GFRK	Glass fiber reinforced plastic
VSV	Variable stator vanes

Symbols
c_p	Pressure coefficient
h	Blade span (mm)
l	Chord length (mm)
Ma	Mach number (–)
n	Rotational speed (min^{-1})
q	Dynamic pressure (Pa)

✉ J. H. Krone
  j-h.krone@ifas.tu-bs.de

1 Institute of Jet Propulsion and Turbomachinery, Technische Universität Braunschweig, Hermann-Blenk-Str. 37, 38108 Brunswick, Germany

2 Institute of Composite Structures and Adaptive Systems, Deutsches Zentrum für Luft- und Raumfahrt, Lilienthalplatz 7, 38108 Brunswick, Germany

🅐 Springer

s   Standard deviation (μm)
t   Blade pitch (mm)
w   Flow velocity (m/s)
x   x-coordinate of ATOS-measurements (mm)
y   y-coordinate of ATOS-measurements (mm)
z   z-coordinate of ATOS-measurements (mm)
x_C x-coordinate of cascade (mm)
y_C y-coordinate of cascade (mm)
z_C z-coordinate of cascade (mm)
Δz Displacement variation in z-direction (mm)
B   Flow angle (°)
β_S Probe angle (°)
$\Delta\beta$ Blade turning (°)
ζ_V Total pressure loss (–)
κ Blade angle (°)
$\Delta\kappa$ Blade angle variation (°)
λ Stagger angle (°)
$\Delta\lambda$ Stagger angle variation (°)
σ Solidity (–)
ϕ Camber angle (°)

Subscripts

1, 2   Stations
REF   Reference condition/blade
MAX   Maximum stagger angle condition
MIN   Minimum stagger angle condition
AL   Aerodynamic loading (windtunnel "on")
LE   Leading edge
MFC   Macro fibre composite
pp   Peak-to-peak
TE   Trailing edge

1 Introduction

The compressor blading of civil jet engines consists of rotating airfoils (blades) and non-rotating airfoils (vanes). In general, the design of blades and vanes of a multistage axial jet engine compressor is a compromise between maximum achievable efficiencies at the aerodynamic design point (cruise) and required safety margins at off-design conditions (T/O an landing). The requirement for a stable operation over a wide range of rotational speeds and the aerodynamic coupling of low pressure compressor (LPC) and high pressure compressor (HPC) for two spool engines is a highly complex design task and is covered by passive and active stabilization technologies. A typical active technology is the variable stator vane (VSV) actuation system which adapts the vane stagger angle with regard to current rotational speeds and ambient conditions. By adapting the stagger angle of a vane row, the vane turning is modified and thus the downstream blade incidence can be adjusted. Vane actuation is relatively easy to implement. This is because no rotating components are included and no centrifugal forces have to be considered and thus mechanical loads on vanes are considerably lower than compared to blades. Variable stator vanes are pivoted at hub and shroud and via a lever arm outside the compressor casing all vanes can be adjusted simultaneously in the form of a rigid body motion. The major disadvantages of VSV systems are weight penalties and a complex maintenance and overhaul procedure. Because of that engine manufacturers aim to reduce the number of VSV stages for every new engine design.

In that context, an additional blade actuation system may further enhance off-design performance but compared to vane actuation, blade actuation is much more complex and the technical feasibility is highly questionable. One major problem is that the whole actuation system has to fit into the blade root and disk space and this means that because of the rotational speed centrifugal forces have then to be considered. In general, regarding blade actuation a rigid body motion, as known from the VSV actuation, is not desired. The first reason is that the desired angle variation is much lower than compared to VSV actuation (±40°). This is because of the VSV system which already provides adequate incidence angles for the blades. Apart from that for blade actuation, it is more efficient to adapt blade stagger angle locally and not globally as obtained for a rigid body motion. Especially the blade tip region is of major interest regarding aerodynamic stability and stage efficiency. At this region, the presence of the tip vortex mainly drives blade row losses and stall inception, and thus blade actuation in the tip region may offer wide design possibilities.

To achieve this goal, an actuation technology is needed which is integrated into the blade's surface without adding too much weight. In addition to that a blade-integrated actuation technology offers the possibility not only to adjust the blade stagger angle but also the blade shape which is not achievable via a standard blade root rotation.

Regarding development trends for next generation turbofan engines blade actuation is of rising interest especially for the fan blading, which is the first stage of the low pressure compressor. The reason is that for next generation turbofan concepts bypass ratios will increase up to 12 or even more and consequently fan pressure ratios will further decrease. This decrease in fan pressure ratio leads to a fan system which is more susceptible for instabilities such as stall and flutter [3]. Another consequence of increasing the bypass ratio and therefore fan diameter is a larger nacelle which has significantly increased weight and drag, which compensates partly or even completely the benefits from a higher bypass ratio. Therefore, engine designers investigate the possibilities of designing thinner nacelle profiles and shorter intake lengths reducing drag and saving weight.

Unfortunately, this kind of nacelle design tends more to intake separations especially at crosswind and angle of attack conditions. In that context, fan blade actuation might be another or maybe the most promising field of use.

In general, the major task regarding blade actuation is to develop a system within the rotating components of the compressor. The requirements of such a system are:

1. Actuation during full operational loads
2. Light and compact components
3. High reliability and low maintenance costs
4. Improved efficiency compared to VSV
5. Power transmission from stator to rotor system

In general, blade actuation is a known technique. Especially for low-speed fans this technique is already used, e.g., in air coolers [2]. Nevertheless, there is no system available which fulfills all requirements for use in a civil jet engine.

Previous work on the feasibility of blade actuation in fans of jet engines were, e.g., carried out by Pratt and Whitney in the 1990s [4]. The Advanced Ducted Propulsor was intended to investigate the capability of a variable pitch fan in terms of fuel savings for future ultra-high bypass turbofan engines. Unfortunately, the design was too heavy.

Violette et al. [5] have published another design of a blade actuation system which is more compact and fits into existing fan center bodies.

Nevertheless, the actuation was performed via additional mechanical components which lead to higher weights compared to non-actuated systems and thus part of the advantage is compensated by these weight penalties. Müller presents in [6] and [7] different concepts for morphing compressor blades with a maximum blade thickness of 24 mm for investigations in a compressor cascade experiment. The first concept uses a kinematic chain as described in [8]. The second concept uses pressurized channels which are integrated in a hyperelastic material. In a third concept, they investigated shape memory alloy wires to apply bending moments in the skin.

In [9], actuated stator vanes were investigated with respect to influence the rotor stator interaction under transient inlet conditions due to a pulsed upstream combustion. One of the considered actuation approaches is the use of piezoceramic actuators attached to the vane surfaces. Actuating the Vane close to the eigenfrequency, a peak-to-peak deflection of 7 mm was achieved.

As a concept study Van de Kamp investigates in [10] shape adaptive compressor blades using Macro Fiber Composite Actuators (MFC's) attached to the blade surfaces. The blade has a maximum thickness of 4.2 mm. The combination of high feasible forces together with their very thin structure as well as a relative low weight (because a kinematic is no longer required) is the main advantage of MFC's in this case.

To make first experiences with MFCs integrated into compressor blades in this pre-study a typical subsonic compressor cascade was equipped with surface integrated actuators. The motivation of that study was to understand how geometric characteristics can be affected and which aerodynamic effects occur. The Reynolds number in that experiment is rather representative for HPC rear stages but also good to get a fundamental insight into the blade actuation via MFCs.

2 Blade design and reference simulation

The basic idea behind blade actuation via MFCs is shown in Fig. 1. Based on a reference condition REF which is the center profile the blade stagger angle can be adapted toward conditions MIN and MAX. Due to the blade bearing the profile leading edge geometry and orientation remains unchanged because it is mechanically fixed. Of course other pivot points can be realized too but for the investigations in this paper the leading edge was defined to be the pivot point. By modifying the stagger angle λ flow parameters like flow angle β_2, camber angle ϕ and flow velocity w_2 change. For higher stagger angles (MAX), the blade camber angle and the blade turning (β_1–β_2) decrease and thus flow velocity w_2 increases which in turn leads to a lower static pressure rise. The significant advantage of such an adaptation is that blade stagger and camber angle can be modified in terms of current blade operation which might be an effective tool during off-design conditions. The object of the investigation in this paper was to quantify the fundamental 2D effects which are obtained for a setup shown in Fig. 4. Therefore, a standard cascade experiment was chosen to be the most effective pre-study setup. A further advantage of a cascade experiment is the optical access regarding deformation measurements. Within a rotating machinery, the optical access is highly limited and
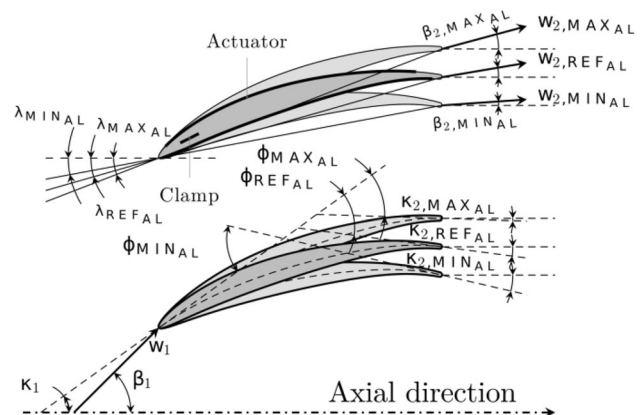

Fig. 1 Principle of blade actuation [14]

because of the blade rotation the deformation measurements are much more difficult to conduct.

2.1 Aerodynamic design and performance

Since the experimental investigation was carried out in a low-speed cascade wind tunnel, the blade profile is based on a typical low-speed NACA-65 series design. The basic NACA profile was modified using an in-house optimization tool to increase profile performance toward high incidences. The investigated profile is shown in Fig. 1. The corresponding loss and blade turning distributions are shown in Fig. 2. The main geometric and aerodynamic characteristics are summarized in Table 1. Compared to the typical NACA-65 design, the blade turning $\Delta\beta = \beta_2 - \beta_1$ is higher and total pressure losses are lower for flow angles β_1 above approximately 40°. The reason for that kind of optimization was to shift flow separations on the blade suction side toward higher incidences. Because of uncertainties of the actuation performance at the very beginning of that project, it was decided to enlarge the operating range and thus to obtain a more stable profile at high incidences. The result is a profile with a relatively low diffusion factor which is actually not representing engine conditions.

2.2 Reference simulation

To have some kind of reference, two different CFD simulations were performed in advance of the experiments. The first setup is a 2D simulation of the nominal profile without any actuation. The results of that simulation represent a perfect unactuated profile without sidewall effects.
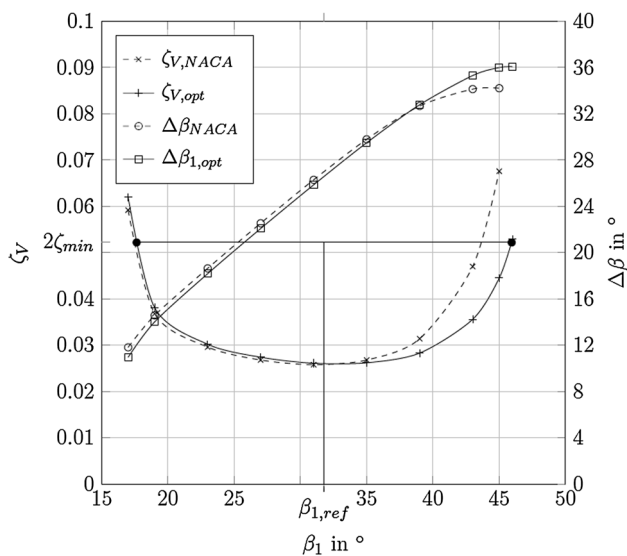
As mentioned above, the manufacturing process was not comparable to conventional blade manufacturing. Because of that, the final geometry of the manufactured blades was assumed to have some influence on the aerodynamics. To quantify that influence between an ideal 2D simulation of the nominal profile and the manufactured blades, all five manufactured blades were digitalized via fringe projection and then a 3D CAD model was created by reverse engineering. In the next step these five CAD models representing the five individual blades were then meshed and solved with RANS. All meshes were block-structured meshes using an OH—topology and simulated via CFX. The turbulence model was a standard SST model without transition. The results are used for comparison purposes in Sect. 4.2.

Table 1 Profile characteristics

Blade characteristic	Value
Chord length (l)	100 mm
Blade span (h)	200 mm
Blade pitch (t)	80 mm
Max. blade thickness	8.6 mm
Stagger angle (λ)	16°
Blade angle (κ_1)	36°
Blade angle (κ_2)	7.5°
Camber angle (ϕ	43.5°
Solidity (σ)	1.25
Blade height ratio (h/l	2.5
Reference inlet flow angle ($\beta_{1,ref}$)	32°
Incoming velocity (w_1)	44 m/s
Reynolds number Re_l based on l	594 000
Blade inlet mach number (Ma_1)	0.13
Blade turning ($\Delta\beta$)	25°
Diffusion factor	0.37

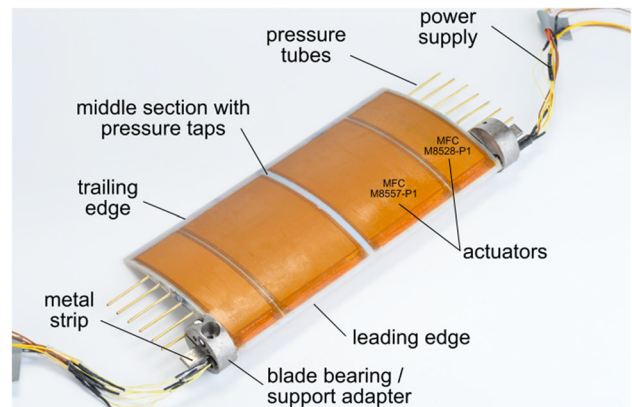**Fig. 2** Profile performance predicted by CFD [16]

Fig. 3 Suction side of the manufactured blade with attached piezoceramic actuators

2.3 Mechanical blade design

In Fig. 3, the blade design is shown. The compressor blades are manufactured via a rapid prototyping process (Poly Jet Modeling) using a photo-polymeric material. A metal strip is integrated over the entire span at the blade's fixed-point close to the leading edge and is used to stiffen the leading edge as well as to carry the blade loads. The blades have two recesses each on the suction and pressure side. One piezoceramic actuator of type MFC M8557-P1 and one of type MFC M8528-P1 is attached to the surface of each recess. Exciting the actuators with a positive or negative DC voltage, the actuators expand or contract, respectively. To realize the required blade bending for different shape conditions and to maximize the available blade deformations the actuators at the suction and pressure side were excited simultaneously with contrary voltages. In this way, the blade deformation described in Fig. 1 can be realized.

To get a smooth surface, the blades surfaces are finished with a thin foil typically used for model building. With a span of 199 mm, the blades are 1 mm shorter than the test section width. Therefore, blade rubbing at the sidewalls is avoided. Only in the area of the leading edges, the blades have contact with the support adapter which is connected to the side walls. Further information to the blade design is given in [11] and [12]. It is important to emphasize that all blades of the cascade were equipped with the same actuation technology to get a simultaneous actuation and therefore keep periodicity during all operating points.

3 Experimental setup

3.1 General setup

For these investigations, a small subsonic cascade wind tunnel of the Institute of Jet Propulsion and Turbomachinery (IFAS) was used (see Figs. 4, 5). This wind tunnel is mainly used for studies on low aspect-ratio blades as well as pre-design investigations since the low operation forces on the blade surfaces allow for the usage of less expensive materials, e.g., polymeric materials. Furthermore, due to the relatively small dimensions pre-studies can be conducted quick and with low costs compared to large cascade wind tunnels. The wind tunnel used for this investigation consists of a radial blower, a settling chamber including screens and a flow straightener, a 2D contraction and the test section where the cascade is mounted. As usual for cascade wind tunnels, a secondary air system is included which removes the boundary layers coming from the
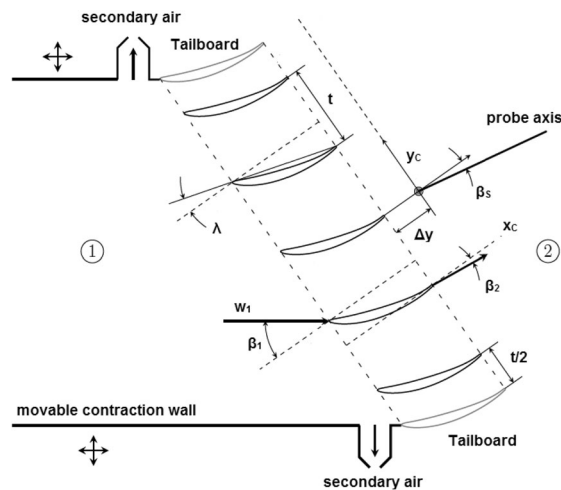

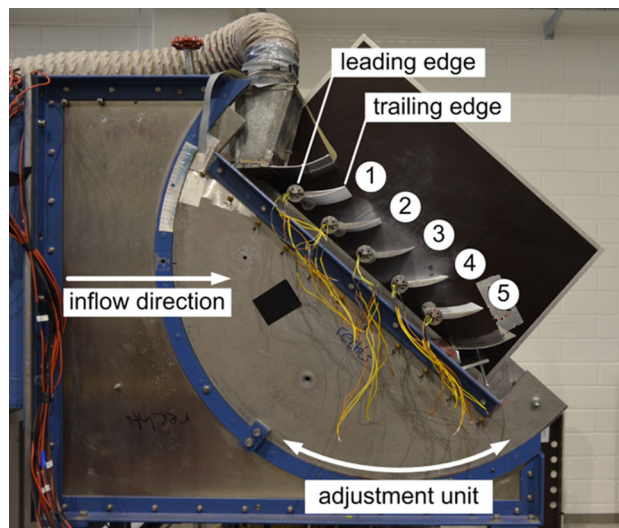**Fig. 4** Experimental setup [14]

Fig. 5 Small cascade wind tunnel equipped with shape adaptive compressor blades and their numbers

contraction. In addition to that, the contraction walls are movable so that the contraction area ratio can be adjusted with regard to the desired flow angle β_1. The flow angle β_1 is simply adjusted by rotating the whole test section assembly (compare Fig. 5).

In typical arrangements, all blades of the cascade are fixed to the sidewalls (wooden wall in the background of Fig. 5). In this special case, the blade mounting had to be realized different because of the actuation requirements. To allow relative movements between each blade and the sidewalls, a small clearance was required. Only in the area of the leading edge, the support metal strip provides the connection between blade and support adapter mounted in the sidewall. The metal strip and the mounting adapter are shown in Fig. 3.

3.2 Measurement of flow quantities and deformations

Flow quantities such as velocities, pressures, and flow angles downstream of the cascade were measured via a 5-Hole-probe. The distance between probe and trailing edge of the cascade was about $\Delta y = 0.3 \cdot l$ which was chosen with respect to an adequate wake resolution and low mixing effects between trailing edge and probe. The measurement uncertainty of the flow angle measurement was in the range of $\pm 0.2°$. For the final wake evaluations, the probe was positioned at 50% blade span. Due to clearance effects at the sidewalls, this position was assumed to be the most representative by minimizing the clearance influence. Actually, a blade height ratio of 2.5 is too small to obtain a perfect periodicity. Especially, the side wall clearances which were needed to allow blade deformation have produced vortices and therefore even midspan values might be influenced somehow. However, because of the limited budget it was not possible to manufacture larger blades and thus the compromise between blade size and budget was accepted for this investigation. In general, before conducting the final wake evaluations the periodicity was checked by traversing along all pitches with a lower point density than for the final wake measurements. Once periodicity was considered to be good enough, the final wake evaluation was conducted along one pitch downstream of the center blade 3. Apart from wake evaluations, blade 2 and 4 were equipped with pressure tappings for measuring the c_p—distribution on the blade's surface. Blade 2 was equipped with pressure tappings on the suction side and blade 4 on the pressure side.

To characterize the resulting aerodynamic results, the blade deformations induced by the actuators as well as the deformations induced by the flow itself are of special interest. For this reason the resulting blade shapes for each actuation and for each flow angle were measured with an optical measuring system (ATOS) using a fringe projection. The measurement uncertainties for this system are determined from the manufacturer by measuring the distance between 2 reference spheres with a defined distance to each other. The standard deviation for the used system is $s = 6 \ \mu m$.

The blade surfaces are measured from different perspectives so that nearly the whole surfaces can be detected. Using the described measuring system, two restrictions have to be noticed. First, the region around the leading edges cannot be measured due to the limited optical accessibility of the wind tunnel. Second, it was not possible to detect the whole blade trailing edge in one single shot. To get the contour of the whole trailing edge, many shots with small detected areas have to be combined in a subsequent post-process. This results in low measuring accuracies directly at the trailing edge. Hence, the trailing edge displacements are not evaluated directly at the trailing edge. The trailing edge evaluations are done with the data from points 5 mm upstream to the trailing edge, which do not make any difference for the trends. The blade angle κ_2 is calculated from measuring points with a distance of 3 mm and 5 mm to the real trailing edge. The used measuring planes for trailing edge and middle section displacements are presented in Fig. 6.

3.3 Experimental procedure

Compared to typical wake evaluations for compressor cascades, the experimental procedure for these investigations was more complex. The reason was that the accuracy of the open loop shape control, which was used here, might influence the aerodynamic results. Reasons for this can be found in [13]. An overview about the experimental procedure and measured shape conditions is given in Table 2. In general, AL indicates that during these experiments the wind tunnel was turned on whereas all conditions without AL were experiments without any flow and thus aerodynamic loads. The applied actuator voltages for all conditions on pressure and suction side are presented in Table 3.
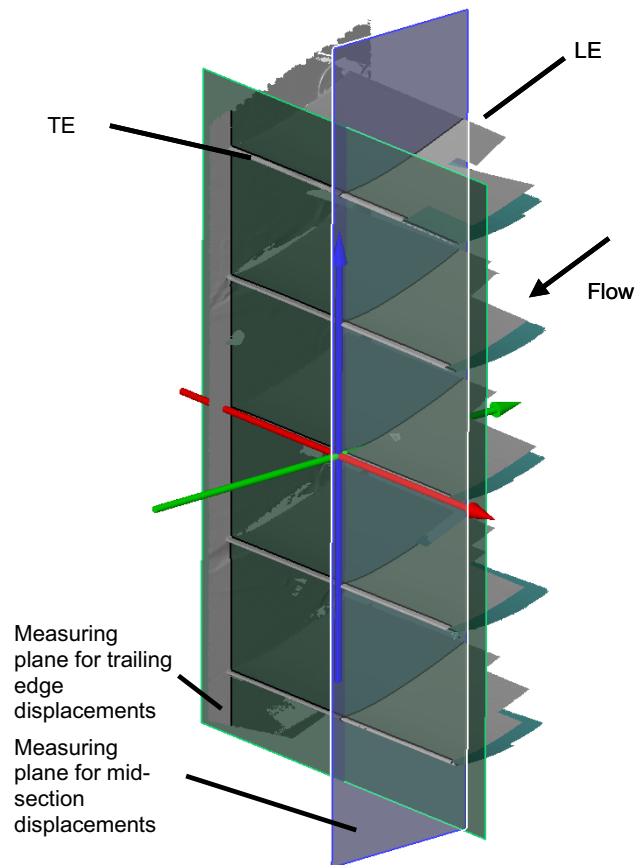

Fig. 6 Measuring planes for detailed deformation analysis

Table 2 Summary of all measurement runs which were performed for each flow angle

No.	Flow	Cond.	Ref. run	Measure-ments
1	Off	0	No	Geometry
2	On	0_{AL}	No	Wake
				c_p
				Geometry
3	Off	REF	Yes	Geometry
4	On	REF_{AL}	No	Geometry wake
				c_p
5	On	REF_{AL}	No	Geometry
6	Off	MIN	Yes	Geometry
7	On	MIN_{AL}	No	Geometry wake
				c_p
8	On	MIN_{AL}	No	Geometry
9	Off	MAX	Yes	Geometry
10	On	MAX_{AL}	No	Geometry wake
				c_p
11	On	MAX_{AL}	No	Geometry

Table 3 Applied voltages to the actuators for each blade condition

Condition	U (V) suction side	U (V) pressure side
REF, REF_{AL}	500	500
MIN, MIN_{AL}	1400	−400
MAX, MAX_{AL}	−400	1400

As a first step condition 0 with short-circuited actuators was investigated. This condition was used to check and to adjust the periodicity of the wakes. The conditions MIN and MAX represent the maximum actuation in both directions. At condition MIN, the actuation leads to minimum stagger angle and maximum camber angle. At condition MAX, the actuation leads to maximum stagger angle and minimum camber angle. Condition REF describes the reference shape for all of the following evaluations and is not equivalent to the short-circuited shape (condition 0). This has mainly two reasons. The first reason is the need for a reference run (described in the following section) which cannot be performed with short-circuited actuators. As a result, the influence of effects like different remnant strains of the actuators induced by different applied voltages of previous investigations cannot be minimized. Second, the suction and pressure side actuators did not have the same influence on the blades deformation. Therefore, as a reference, the actuators were excited with a DC voltage of 500 V on both sides which corresponds to the middle of the actuators DC voltages range from −400 to 1400 V.

The reference run was intended to minimize the influence of the applied voltages history. Further information is given in [13]. The reference run is a sinus wave with 15 oscillations, an amplitude of 1800 Vpp and an offset of 500 V at each actuator. The period length is 10 s. After these 15 oscillations, the voltage signal stops at the corresponding DC voltage given in Table 3. In condition MIN and MAX, the actuators were applied with different DC voltages. Therefore, in these cases, the reference run was done with a phase shift of 180° between the suction and pressure side actuators.

For each condition the procedure was as shown in Table 2. First, the cascade geometry was measured without any aerodynamic loads. After that the wind tunnel was switched on and the geometry was measured again. After that all aerodynamic quantities like wake evaluation and pressure distributions were measured. Because of the measurement duration for evaluating the wake, the geometry was again measured after completing the wake evaluation. This was done to obtain potential geometry drifts occurred during the wake evaluation.

3.4 Drift evaluation

Since the outer shape of the blades is essential for the flow conditions in the cascade, a large effort was spent on the experimental determination of the blade's geometries and deformations. Please note that the presented geometry results of REF_{AL}, MIN_{AL}, and MAX_{AL} only describe the conditions of number 4, 7, and 10 (compare Table 2). The results of number 5, 8, and 11 are not presented, because for each flow angle two geometric measurements exist for the same conditions.

Figure 7 gives an overview about the resulting shape conditions at the mid-section trailing edge of blade 3. At this point, the focus is on geometry measurements before and after wake and c_p measurements. The shape variations at condition REF_{AL} (No. 4 and No. 5) and MAX_{AL} (No. 10 and No. 11) before and after aerodynamic measurements are almost $\Delta z \approx 0$ mm. For condition MIN_{AL}, a short deviation between No. 7 and No. 8 is observed. In comparison to the actuator-induced displacements between condition MIN-REF and MAX-REF, the observed deformation is considerably smaller. Hence, the measurements after wake and c_p are not considered. The reason for this behavior is material creep and a drift by applying the actuators with a DC voltage. A detailed discussion to this topic is given in Sect. 4.1.1.

During the deformation measurements the suction side as well as the pressure side was measured, but for the following evaluations only the pressure side is used. This is justified with a constant blade thickness. Considering the actuated blades similar to a bended beam, the local blade
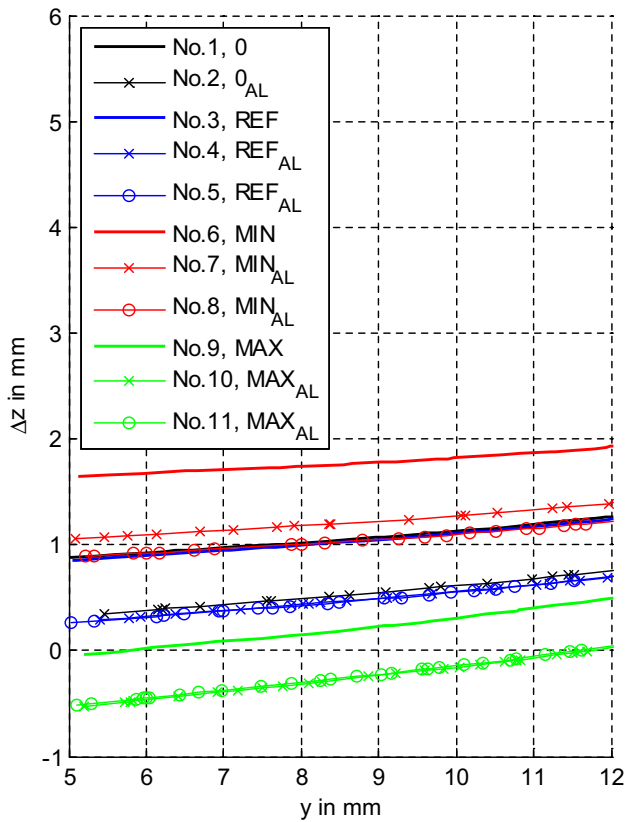
Fig. 7 Pressure side contour at the middle section trailing edge of blade 3 in different shape conditions for flow angle $\beta_1 = 30°$

Table 4 Blade pitches at the trailing edge in mounted state for $\beta_1 = 30°$ measured in condition 0

Pitch no.	Pitch in mm
Pitch 1 (blade 1 to blade 2)	78.64
Pitch 2 (blade 2 to blade 3)	80.28
Pitch 3 (blade 3 to blade 4)	79.96
Pitch 4 (blade 4 to blade 5)	81.69

were not directly screwed on the sidewalls. Each blade has a support metal strip which is attached to the sidewall adapters. Since it is not possible to compensate geometric deviations within the cascade by a certain wind tunnel setting the periodicity was assumed to be not as good as required for typical cascade experiments.

With the described surface measurements, the distance between the blades at the trailing edge (pitches) is determined. With these results, it is possible to characterize the real pitch of the blades in mounted state. The results are given in Table 4. The averaged blade pitch over all blades measured at the midpoint of the trailing edge is 80.14 mm instead of 80 mm.

Compared to typical experimental setups for cascade experiments, these geometric deviations in pitch are relatively high. But regarding the individual manufacturing process for the blades and especially because of the blade bearing this deviations were considered to be good enough to show the effects of deformable blades.

Detailed actuator-induced blade deformations as well as aerodynamic-induced blade deformations are presented in the following sections.

cross-sections rotate and the blade shape changes, but the local blade thickness stays constant. Consequently, the pressure and suction side deformation behaves identically. This assumption allows the evaluation of only the pressure side.

3.5 Alignment check

In general, for standard cascade experiments deviations of blade shape within the blade set are small and in the range of the manufacturing tolerance. For standard milled blades, the accuracy is in the range of 0.01 mm. Together with standard blade mounting on the sidewalls, the geometric deviation from target state is 0.1 mm in maximum. That means that during the experiment there is almost no geometric effect on the periodicity and thus a periodic condition is achieved by adjusting the wind tunnel (boundary layer suction system and tailboards).

For the actual investigations, geometric deviations were considered to be on a higher level. The reason for that is the above described manufacturing process of the blades. Although using the same process and materials, the results are five individual manufactured blades. In addition to that, blade alignment was much more difficult since the blades

4 Results

4.1 Actuator-induced blade deformations

In this section, actuator-induced deformations for both MIN and MAX conditions are presented. These geometries were derived without aerodynamic loads for different flow angles for the sake of repeatability and possible influences from clamping conditions as well as to characterize the blade deforming performance induced by the actuators. The deformations are calculated as the distance (perpendicular to the surface itself) between the blade surfaces of condition MIN using REF as reference (see Fig. 8) and condition MAX against the same reference (see Fig. 9). All results are transformed into the same coordinate system, where the yz-plane is the middle plane between the right and the left wind tunnel wall. The midpoints of the trailing edges of blade 2 and blade 4 define the z-axis. The origin of
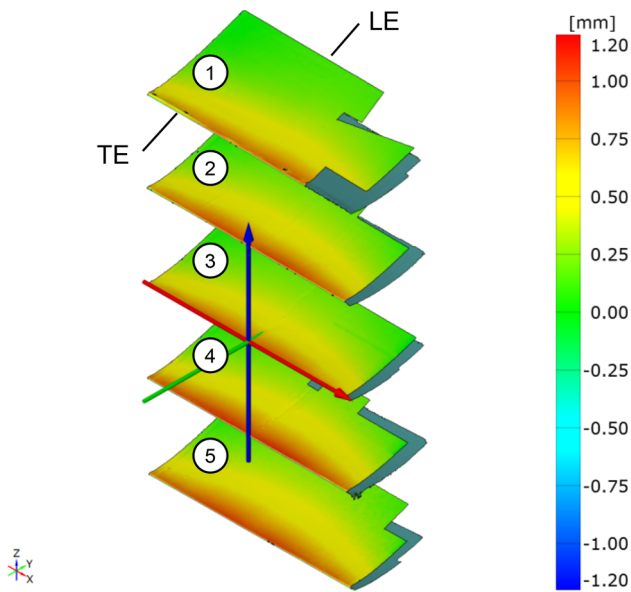
Fig. 8 Actuator-induced blade deformations at the pressure side between condition MIN and REF without flow for $\beta_1 = 30°$
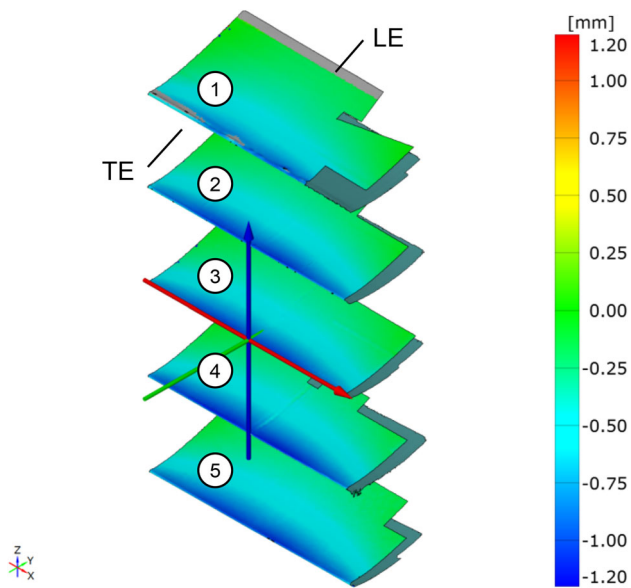

Fig. 9 Actuator-induced blade deformations at the pressure side between condition MAX and REF without flow for $\beta_1 = 30°$

Table 5 Actuator-induced trailing edge displacements averaged over all flow angles for each blade calculated at the middle section ($x = 0$ mm) at $y = 5$ mm between MIN and REF condition

Blade number	1	2	3	4	5
Displace-ment in mm	0.79	0.87	0.80	0.95	0.95
Averaged rel. error in %	3.29	2.52	2.83	1.81	3.41

Table 6 Actuator-induced trailing edge displacements averaged over all flow angles for each blade calculated at the middle section ($x = 0$ mm) at $y = 5$ mm between MAX and REF condition

Blade number	1	2	3	4	5
Displacement in mm	−0.72	−0.84	−0.84	−0.89	−0.86
Averaged rel. error in %	4.97	3.47	3.02	3.66	5.63

Figures 8 and 9 show a view of the pressure side for $\beta_1 = 30°$. Further results for other flow angles are given in the appendix in Figs. 21 and 24. The top blade is blade 1 and the lowest blade is blade 5. All figures have the same scale. Even though all blades should behave similar, comparing all five blades in Fig. 8 shows different blade deformations. In case of $\beta_1 = 30°$ blade 4 has the biggest and blade 1 has the lowest displacement at the trailing edge. Figure 9 shows the same effect but with the sign reversed. To clarify this effect and to compare the available blade deformations of all blades in Tables 5 and 6, the averaged trailing edge displacements at the middle section over all flow angles for each blade with the resulting averaged relative error (these errors can be used as a global error for all measurements of actuator-induced blade deformations) are given. This effect can be explained with manufacturing inaccuracies of the actuators and the resulting performance difference between them. Another point are manufacturing inaccuracies of the blades like different adhesive layer thicknesses between the actuators and the blades as well as process inaccuracies during the rapid prototyping process like irregular material curing and a resultant blade warping.

Looking at the trailing edge displacement distribution along span (x-axis), the results of blade 3 for three different flow angles are given in Fig. 10. To compare the actuator-induced deformations of blade 3 with the remaining four blades, the same plots for these blades are shown in Figs. 37 and 40. To condense the measurements to one meaningful value, the averaged trailing edge displacements over span are given in Table 7.

The displacements along the trailing edge for each condition are not constant which results in a blade warping. The displacements close to the middle section are much larger than those towards the sidewalls. For example the
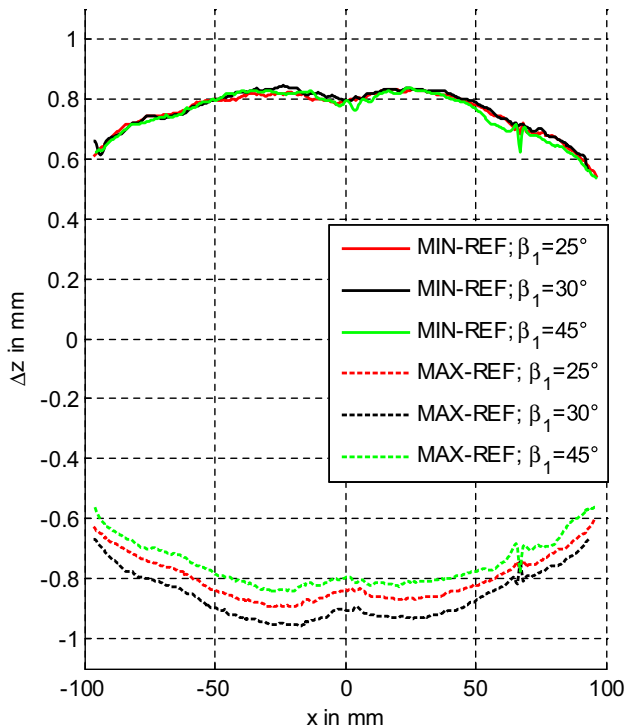
the coordinate system is located at the middle of the trailing edge of blade 3. The resultant x-axis is nearly equal to the trailing edge of blade 3.

Due to the optical accessibility of the cascade and the non-automated measuring process, it was not possible to detect exactly the same blade surfaces for each shape condition. Consequently, a few areas were measured in condition REF but not in condition MIN and MAX. For these areas, the displacements were not calculated and are presented in gray colors.

Fig. 10 Actuator-induced trailing edge displacements of blade 3 at $y = 5$ mm for different flow angles over span (x axis) without aerodynamic loads

Table 7 Averaged trailing edge displacements of blade 3 over span for different flow angles at $y = 5$ mm

Flow angle β_1 in °	25	30	45
MIN-REF	0.76	0.77	0.75
MAX-REF	−0.80	−0.86	−0.75

trailing edge displacement of blade 3 between MIN and REF at middle section is $\Delta z \approx 0.79$ mm and near to the left end the displacement is $\Delta z \approx 0.65$ mm. This may be due to transversal contraction effects of the blade's base material in combination with the actuation of the MFC's. Another reason is passive regions at the blade ends.

Some discontinuities can be found in the blade displacements at the coordinates region 65 mm $\leq \times \leq 70$ mm and -70 mm $\leq \times \leq -65$ mm as well as in the middle section of the blade. This can be explained with the non-actuated regions of the blades, caused by the necessary pressure tappings in the middle section and the passive area between the actuators of type MFC M8557-P1 and MFC M8528-P1 (compare Fig. 3).

Comparing the trailing edge displacements of MIN-REF and MAX-REF, different behavior can be observed. Exciting the actuators at different flow angles without flow should result in the same displacement. The results of

MIN-REF for different flow angles without flow are nearly the same. In contrast to that the results of MAX-REF are unequal although the actuators are applied with the same voltage. For the remaining four blades and in previous preliminary investigations in [10] this can be observed, too, but with different intensity. As described in [10] this behavior has different reasons like a non-linear behavior of the blade material due to creep and a drift by applying the actuators with a DC voltage as described in [12]. Another reason is the measuring time needed to survey the surfaces of all blades in conjunction with the effects described above. Because of the non-automated geometry measuring process the blade's suction and pressure sides were measured in different time intervals. This leads to small deviations of the measured blade's surfaces and the resulting calculated blade deformations. As a consequence, the exciting of piezoceramic actuators for such applications always require a closed loop control. Open loop control is not sufficient.

Comparing the trailing edge deformation of all five blades in general the same behavior can be observed. A detailed comparison shows different achieved blade displacements. As described above, this can be explained with manufacturing inaccuracies and actuator performance differences.

The trailing edge displacements between condition MAX and REF of blade 1 in Fig. 37 show different results as the four remaining blades. This can be explained with high measurement inaccuracies by measuring the blades' trailing edge.

Another measure of interest is the actuator-induced displacement along blade chord. The resulting displacements of blade 3 over chord at middle section ($x = 0$ mm) are shown in Fig. 11. The solid lines describe the measured blade displacements between condition MIN-REF and MAX-REF. To compare the displacements of blade 3 with the displacements of the four remaining blades, an envelope of all five blade deformations is also presented. Plots of the remaining four blades are given in the appendix in Figs. 33 and 36.

With the displacements between MIN-REF and MAX-REF, a camber angle variation due to the excitation of the actuators can be proven. The blade angle variation near to the leading edge can be approximated as $\Delta \kappa_1(-y = 100$ mm$) \approx 0°$. The blade angle variation $\Delta \kappa_2$, which is calculated with the displacements at $y = 3$ mm and $y = 5$ mm, decreases for configuration MIN with $\Delta \kappa_2 \approx -0.98°$ and increases for configuration MAX with $\Delta \kappa_2 \approx 1.37°$. It follows a total blade angle variation of $\Delta \kappa_2 = 2.35°$. Under the assumption of fixed blade angle κ_1 this results in a total camber angle variation of $\Delta \varphi = 2.35°$. The resulting blade angle variation of the remaining four blades at the middle section is given in
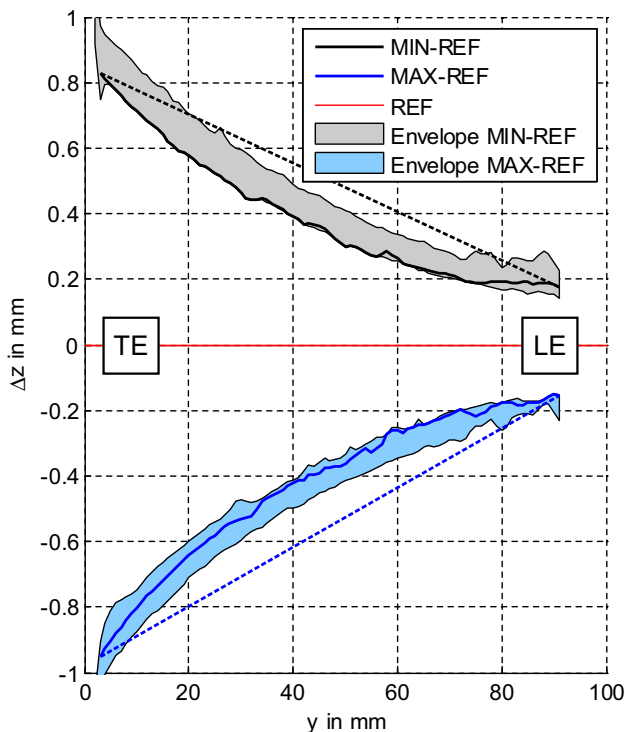
Fig. 11 Actuator-induced displacements Δz at the middle section of the pressure side of blade 3 for $\beta_1 = 30°$ along chord (y); *dashed lines* indicate linear approximation of start and end; *colored surfaces* indicate the envelope of all blades
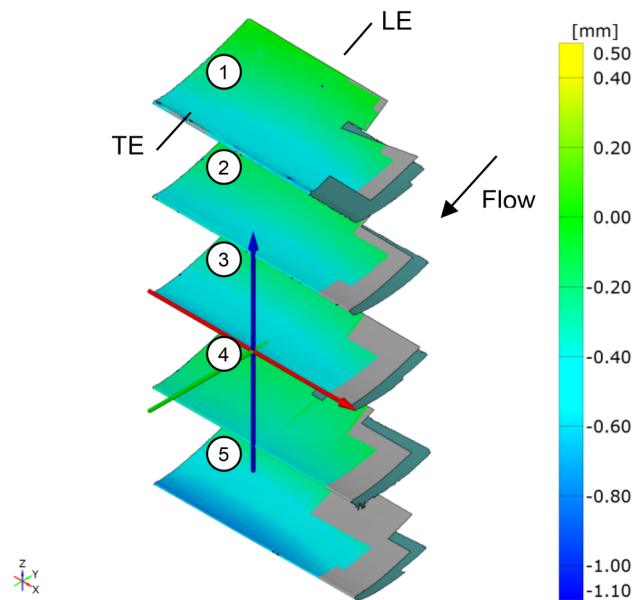

Fig. 12 Blade deformations at the pressure side caused by the flow between condition REF_{AL} and REF for $\beta_1 = 30°$

Table 8 Actuator-induced blade angle variation $\Delta\kappa_2$ of all five blades at the middle section for $\beta_1 = 30°$

Blade number	1	2	3	4	5
Blade angle variation $\Delta\kappa_2$ in °	–	2.37	2.35	2.55	2.40
Deviation from mean value in %	–	−1.99	−2.81	5.46	0.74

Table 8. Due to measurement errors at the trailing edge of blade 1 (see Figs. 33, 37), the blade angle variation of blade 1 is not calculated. The resulting averaged blade angle variation from all blades at middle section is $\Delta\kappa_{2,m} = 2418°$. This results in a maximum deviation from the mean value of 5.46% which is in an acceptable range for the used experimental setup.

4.1.1 Aero-induced blade deformation

Besides, the actuation-induced deflections of the blades caused by the aerodynamic loads are of interest. They are a measure for the inherent stiffness of the blades themselves and have to be taken into account when setting up a simulation for validation using this experimental data. Figure 12 shows the deformations induced by aerodynamics at flow angle $\beta_1 = 30°$. It presents a view of the pressure side,

where the actuators were kept in REF and the deformation results from switching on the wind tunnel. Plots for other flow angles and shape conditions can be found in the appendix in Figs. 25 and 32.

It can be seen that there are differences in the displacements of the blade trailing edges, especially between those of blade 4 and 5. Those differences have to be taken into account, when estimating the periodicity of the aerodynamics.

Looking at the aerodynamically induced trailing edge displacements along span of blade 3 in Fig. 13 and Table 9, a similar trend as for the actuation-induced displacement can be found. It can be recognized that the trailing edges are being deformed toward the suction side (displacement against to the direction of the z-axis) with different displacements on the left and right clamping condition. This can only be explained by different clamping conditions on both sides. Other Clamping conditions with higher rigidity and the possibility for fine alignments with adjusting screws should be developed and implemented in future work.

Furthermore a stronger deflection in the middle than on the sides can be observed which indicates flow induced span-wise bending of the blade. For the conditions MIN_{AL} and MAX_{AL}, this effect can be counteracted with lower voltages at the middle actuators against the outside actuators. In the case of condition REF_{AL}, the middle section actuators have to be excited by low voltages while the outside has to be unactuated. Another option to minimize the observed blade bending is to adjust the bending stiffness in span-wise direction with a discrete material
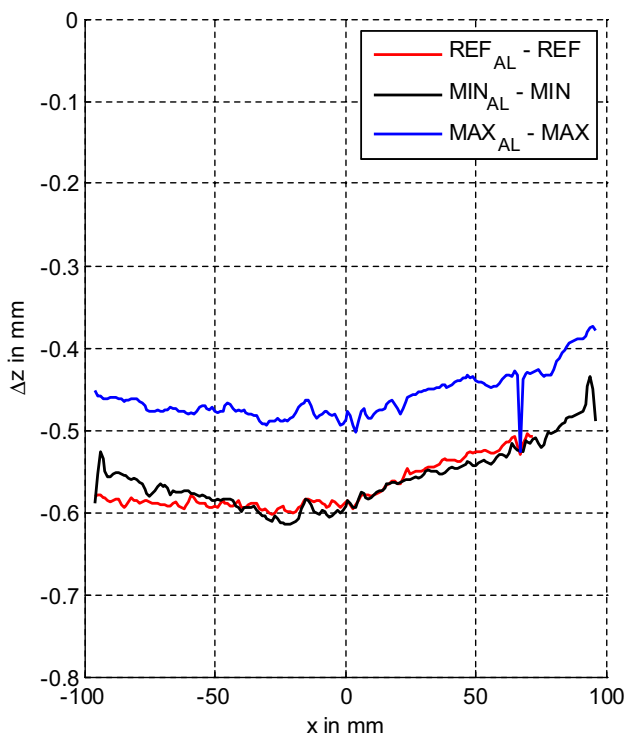
Fig. 13 Trailing edge displacements Δz over span (x axis) of blade 3 at $y = 5$ mm caused by the flow for $\beta_1 = 30°$

Table 9 Averaged trailing edge displacements over span (x axis) of blade 3 at $y = 5$ mm caused by the flow for different flow angles

	25°	30°	45°
MAX$_{AL}$-MAX	−0.55	−0.46	−0.33
REF$_{AL}$-REF	−0.56	−0.57	−0.38
MIN$_{AL}$-MIN	−0.64	−0.56	−0.41

Fig. 14 Trailing edge displacements Δz averaged over span at $y = 5$ mm of blade 3 for different flow angles induced by aerodynamic loads

distribution. Therefore, the already used manufacturing process Poly Jet Modeling can be used.

As seen in Fig. 13 and Table 9, condition MIN shows the largest displacements, whereas condition MAX shows the smallest displacements. This can be explained by the general pressure distribution of the blades. The resultant force of the pressure distribution contributes to the deformation in the direction of the suction side. In the direction of the pressure side, the pressure distribution hinders deformations. Figures 41 and 42 represent the same plots for the flow angles $\beta_1 = 25°$ and $\beta_1 = 45°$.

Figure 14 gives an overview about the averaged trailing edge displacements over span of blade 3 for different shape conditions and for different angles of attack. The overall trends as described with Fig. 13 are the same, but the level of deflection is increasing with reduction of the flow angle. It is emphasized again, that the deflection is higher with lower blade loading. The reason for that behavior can be

explained by the pressure distributions. Increasing flow angles lead to more front loaded pressure distributions which in turn lead to a shift of the point of attack of the lift upstream toward the leading edge. Hence, the lever arm between lift and fixed leading edge decreases and although lift is higher trailing edge deflection decreases compared to lower flow angle.

As seen in Fig. 14, there are outliers from the general trend at lower angles of attack. Further investigations to identify the cause are required and are part of future work.

The aerodynamic-induced displacement along chord for blade 3 can be found in Fig. 15. All curves can be approximated linear (dashed lines). The induced displacements for REF$_{AL}$-REF and MIN$_{AL}$-MIN result in a stagger angle variation of $\Delta\lambda \approx 0.38°$ and $\Delta\lambda \approx 0.37°$, respectively. Caused by the decreased camber angle in condition MAX, the pressure coefficient decreases (compare with Fig. 20). This leads to a lower stagger angle variation with $\Delta\lambda \approx 0.24°$. The linear nature of the displacements shows that a rotation of the overall profile is the dominating shape change, rather than an aerodynamic-induced change in camber.

Summarizing the results above, the effects under aerodynamic loads are not negligible. The described displacements and the resulting influence to the periodicity should
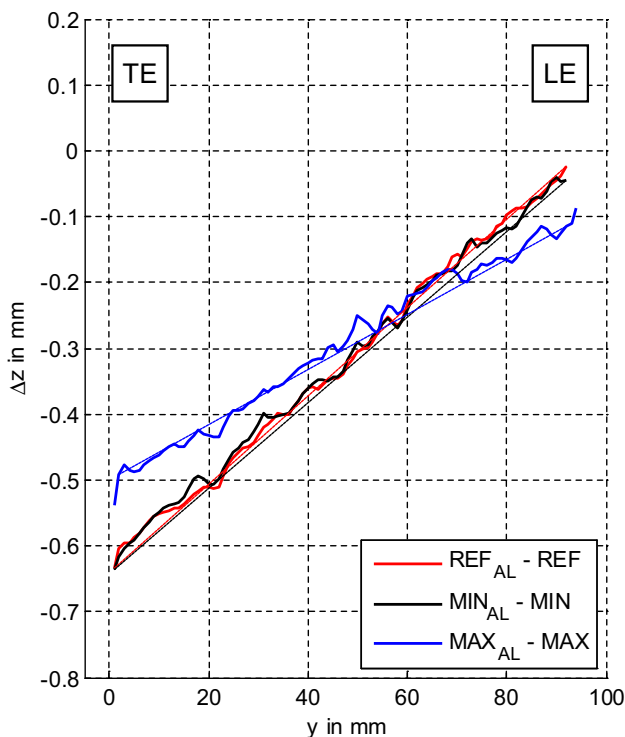
Fig. 15 Displacements Δz at the middle section of blade 3 for $\beta_1 = 30°$ over span (y) induced by aerodynamic loads
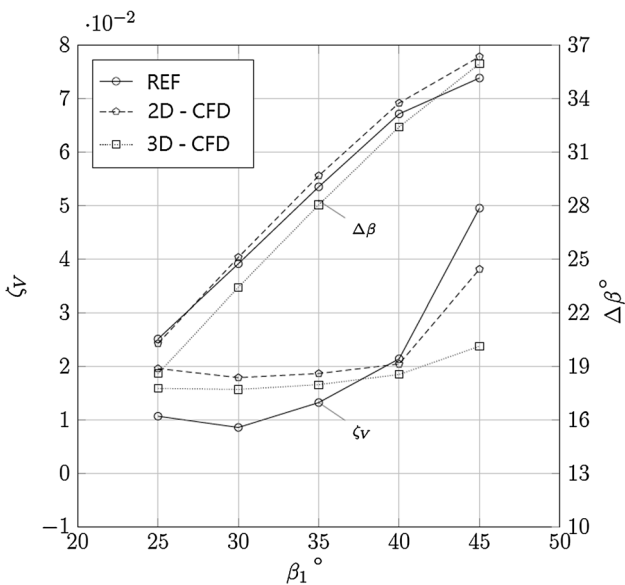

Fig. 16 Comparison of 2D and 3D—CFD with the experimental data obtained for the REF—condition [14]

be considered in the following aerodynamic evaluations. However, using materials from real fan blade applications (for example CFRP or titan alloys) the expected blade deformation under aerodynamic loads should be much less than the observed.
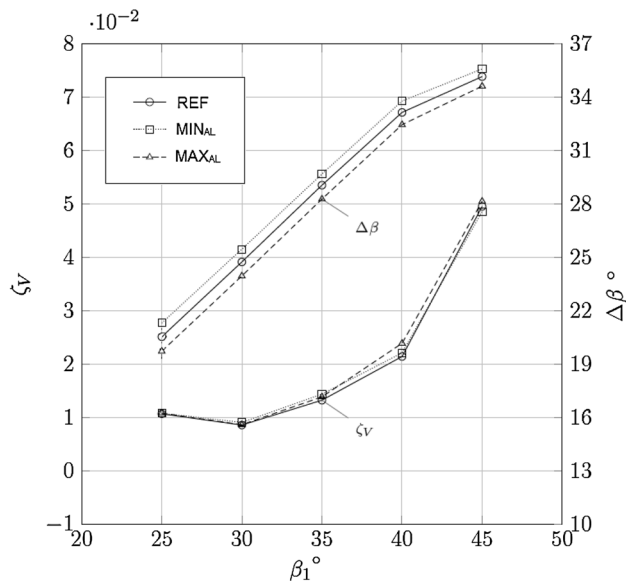

Fig. 17 Experimental turning and loss distributions for REF, MIN$_{AL}$, and MAX$_{AL}$ conditions [14]

4.2 Flow measurements

4.2.1 Blade turning and loss distributions

In general, blade turning of the REF condition in the experiment and the CFD simulations (Fig. 16) is in good agreement. The difference of the predicted and measured turning is within a tolerance of approximately 2° which is good with regard to the list of uncertainties.

In Fig. 17, the mass-averaged blade turning $\Delta\beta$ and the loss coefficients ζ_V are shown for each flow angle. Regarding Table 2, three measurements for each angle are plotted. REF (No. 4) is the non-actuated zero-position condition, MIN$_{AL}$ (No. 7) is the minimum stagger angle condition and MAX$_{AL}$ (No. 10) is the maximum stagger angle condition.

From the experiment, it can be seen that the actuator system is able to increase and to decrease blade turning $\Delta\beta$ over the entire operating range with an approximately constant margin.

Close to the reference inlet flow angle at $\beta_1 = 30°$, the turning can be reduced about $\Delta\beta = -0.8°$ at condition MAX$_{AL}$. This can be explained by the increased stagger angle due to the actuation. The maximum increase of 0.8° of the turning $\Delta\beta$ is reached at $\beta_1 = 25°$ at condition MIN$_{AL}$. Toward higher blade inlet angles, the ability of the actuators to affect the turning decreases slightly. At part load condition ($\beta_1 = 45°$), the turning increase is 0.4° at MIN$_{AL}$ condition while a decrease of 0.5° is measured at MAX$_{AL}$ condition.

The decreasing ability to affect the blade turning angle at higher flow angles can be explained by the progressively increasing aerodynamic load at the suction side of each blade. High inlet flow angles result in high incidence angles and consequently increased turnings. At higher incidence angles, the deceleration at the suction side increases significantly and thus the boundary layer thickens. As a consequence, the effective curvature of the blade decreases due to the thicker boundary layer and an increase or decrease of the curvature because the actuators become less effective. Furthermore, the flow around the blades tends to seperation, which would cause the actuator to have a lower effect on the turning angle, too.

The profile total pressure losses in Fig. 17 are defined as:

$$\xi V = \frac{pt1 - pt2}{q1}.$$

The loss coefficients of the experiment are on a considerably lower level than obtained for the 2D and 3D CFD prediction. Only at $\beta_1 = 40°$ the pressure loss coefficient is on the expected level. The only explanation for that result is that strong sidewall effects have led to increased dynamic pressures downstream of the cascade which in turn leads to artificial lower pressure losses. Nevertheless, blade actuation has no significant influence on the pressure losses. In this case, total pressure losses are within the measurement uncertainties of the pressure acquisition system. Therefore, no explicit statement about the influence of the actuation on the aerodynamic losses can be made. On the other hand, obviously for such low aerodynamic loadings blade turning can be adapted without any penalties in pressure loss, which is an interesting degree of freedom for designers.

4.2.2 Periodicity of the cascade flow

To obtain physically meaningful local distributions of an infinite cascade, the periodicity of the wake downstream of the cascade, which consists of five blades and therefore four pitches, was measured for each flow angle. For all angles, the distribution of the flow angle β_2 is shown in Fig. 18. In general, periodicity is acceptable for the inner two pitches (-80 mm $< y_C < 80$ mm). For the outer two pitches ($-160 < y_C < -80$; $80 < y_C < 160$), the quality of periodicity decreases. Furthermore, the higher the flow angle β_1 the higher the deviations are found in terms of β_2. The reason for the deviations of the individual wake peaks is mainly the coarse resolution for the periodicity check and thus the peaks do not contribute to the periodicity check. Nevertheless, for the inner two pitches the quality was assumed to be good enough for evaluating the actuation effects for this experiment. It is important to mention that periodicity was only checked for the REF conditions
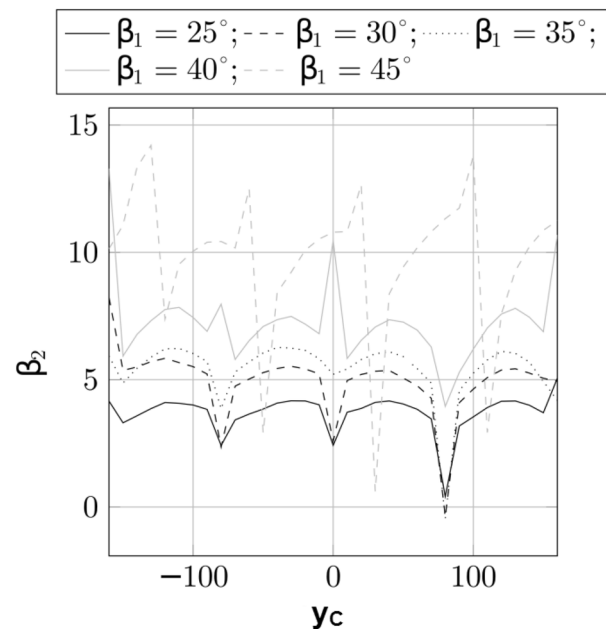

Fig. 18 Measured flow angle periodicity of the cascade flow [14]

and not again for the actuated conditions. This decision was made because of the relatively small influence of the actuation on the flow and thus it was assumed that periodicity is good for the actuated conditions, too.

In addition to the presented angle β_2, the dimensionless pressure rise was taken as a measure of the periodicity as well as the flow angle β_2. Only if both, the outflow angle and the dimensionless pressure rise, were sufficiently periodic, the detailed measurements were started.

4.2.3 Local blade turning

The global compressor cascade characteristics previously shown are based on local quantities taken at 81 positions across one pitch of the center blade. In Fig. 19, the local blade turning $\Delta\beta$ is shown for the reference condition REF$_{AL}$(solid line) and the maximum deformation conditions MIN$_{AL}$(dashed lines) and MAX$_{AL}$(dotted lines). With respect to clarity, the symbols for the actuated conditions are not shown. With regard to a clear overview, over the local behavior of the flow downstream of the cascade, local distributions are plotted for three flow angles only. As expected, the higher the angle the thicker the wake of each profile is. The wake is clearly indicated by the high and low peaks of each distribution.

Higher aerodynamic loads at high flow angles lead to thicker boundary layers on both pressure and suction side and hence wider wakes. Furthermore, thicker boundary layers especially on the profile suction side reduce the effective blade curvature and thus the actuation effect decreases significantly across the whole passage. This
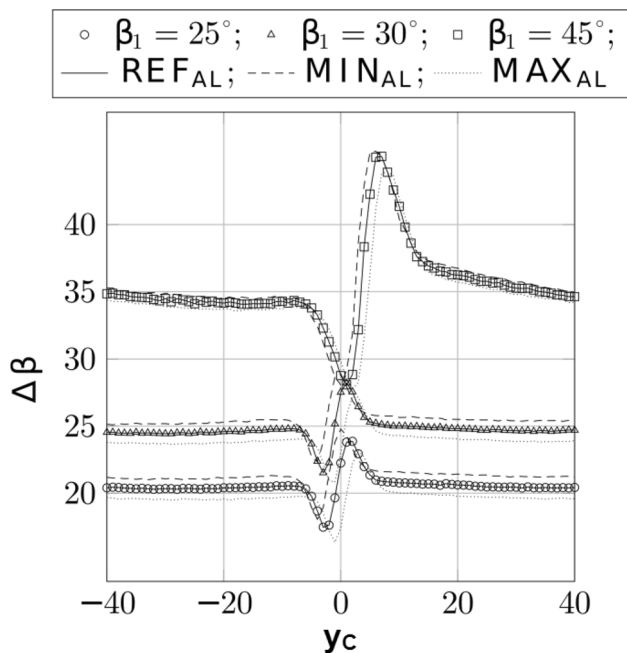
Fig. 19 Measured local turning values at flow angles $\beta_1 = 25°$, 30°, and 45° [14]

Fig. 20 Pressure distributions at flow angles $\beta_1 = 25°$, 30°, and 45° [14]

becomes more clear when the local distributions of the blade turning angle at $\beta_1 = 30°$ is compared to the local quantities at $\beta_1 = 45°$. At an inflow angle of 30° which is close to the reference inflow angle blade turning can be effectively manipulated across the whole passage. This is indicated by an approximately constant margin between REF_{AL}, MIN_{AL}, and MAX_{AL} deformation conditions. Further away from the reference inflow angle, at $\beta_1 = 45°$, the effect of the actuator is still measurable and clearly present, but less distinct due to the thicker boundary layer, especially on the highly loaded suction side.

At condition MIN_{AL}, at which the blades' stagger angle is decreased compared to the REF condition, the blade turning increases over the whole range of the measured inflow angles. In contrast at condition MAX, which is characterized by a decreased higher stagger angle, the turning decreases. Therefore, it can be concluded that the aerodynamic load, which is a consequence of the flow turning, can be increased at deformation condition MIN_{AL} and decreased at deformation condition MAX_{AL}. Furthermore, for the chosen profile there is no influence of blade actuation on the width of the wake for a fixed flow angle. The reason for that is the profile characteristic with only small changes in pressure loss over a wide range of inlet flow angles.

4.2.4 Pressure distributions

In addition to the wake measurements, the pressure distributions at each flow angle and for each deformation condition have been measured as well. In Fig. 20, the pressure distributions measured at $\beta_1 = 25°$, 30°, and 45° are presented. To make the diagram easier to read symbols are only shown for the REF condition. The pressure coefficient was calculated by:

$$cp = \frac{p - p1}{q1},$$

where p is the local static pressure on the blade surface. Unfortunately, due to the blade bearing design there were no pressure tappings possible between $0 < x_C/l < 0.2$. Nevertheless, the area between $0.2 < x_C/l < 0.8$ has a resolution of $x_C/l = 0.05$ which allows for some important conclusions. In general, c_p—measurements were performed several times and the repeatability was in an acceptable range. From these results, it was concluded that pressure tappings are not influenced by the actuation in terms of cracks and thus leakage.

Obviously, the pressure side of the blades can be affected at both deformation states compared to the non-actuated condition. In general, higher turning (MIN_{AL}) leads to higher c_p-values, whereas a decreased turning (MAX_{AL}) leads to lower c_p-values. This effect is more or less constant along the profile. Furthermore, at $\beta_1 = 45°$ the characteristic of the distribution is significantly different from the other distributions. Due to the high flow angle, the profile becomes strongly front loaded which leads to high c_p-values toward the leading edge of the profile. Nevertheless, the actuation effect is still in the same range as for lower flow angles.

In contrast, for $\beta_1 = 25°$ and $\beta_1 = 30°$ the suction side of the blades is only significantly affected when the stagger angle at condition MAX_{AL} is increased and therefore turning is decreased. The change in c_p is then of the same magnitude as obtained on the pressure side and is again constant along the profile. Increasing the turning at condition MIN has no influence on the c_p—distributions of the suction side. At $y/l = 0.5$ there is a noticeable discontinuity indicating laminar to turbulent transition of the boundary layer.

At $\beta_1 = 45°$ this trend vanishes. Due to the relatively high turning and thus thicker boundary layers, the actuation has no noticeable effect on pressure distribution on the suction side. As obtained on the pressure side, the characteristic of the distribution differs significantly from the lower flow angles. Due to the high angle, the profile becomes strongly front loaded which is indicated by the more or less constant positive slope and low c_p-values towards the leading edge. If there were pressure tappings between $0 < x_C/l < 0.2$ a strong suction peak would be measured.

5 Conclusions

In this paper, the results of a wind tunnel cascade experiment with five shape adaptive compressor blades using piezoceramic actuators are presented. The structural feasibility of the adaptive blades was demonstrated with a total camber angle variation of $2.35°$. Furthermore, the blade deformations induced by aerodynamic loads were extracted. These data were recorded and discussed for a range of flow angles between $\beta_1 = 25°$ and $\beta_1 = 45°$. From a mechanical point of view the major conclusion is that a deformation in the desired order of magnitude under aerodynamic loading is possible.

It was found that the deformations due to the actuators alone were non-periodic. Slight differences in the performance of the different actuators contributed to this result. Either a more careful selection of the actuators or a prior characterization and associated compensation could improve the periodicity of deformation. Closed-loop control may also alleviate this problem.

It was discovered that the aerodynamic-induced deformation results are non-uniform along the span. This can be improved by tailoring the actuator voltage based on their span-wise position, and/or tailoring the material bending stiffness along the span, for example by placing voids in the structure at appropriate locations or using multiple materials with differing stiffnesses.

A major lesson learned is that future investigations of morphing fan blades using this concept with static blade deformations need a closed loop control to ensure the periodicity between the blades. Another possibility to ensure the periodicity is to improve the manufacturing process (for example using CFRP as the blade material the actuators can be integrated directly in the prepreg which results in a constant adhesive layer thickness).

For future investigations, this technology could be transferred to active twist fan blades with static blade deformations. From the electrical point of view the actuators work as capacitors. Hence, the needed electrical power for static twist deformations is low and thereby additional masses for the power supply are also low.

From the aerodynamic point of view, wake evaluations have proven, that this kind of actuation system is able to manipulate blade turning for a given flow angle in the range of $\pm 1°$. It is important to emphasize that this result is only valid for the blade architecture and materials used in this investigation. Furthermore, the aerodynamic loading was chosen relatively small because of some uncertainties of the actuator performance in the beginning of that project. Further investigations have to quantify whether the effect is in the same range for high loadings as typical for real engine applications.

A major result is that for the chosen profile the ability of changing flow quantities like flow angle is approximately constant over the whole operating range. Moreover, there is no significant influence on profile total pressure losses. In that context it is important to note, that the chosen profile was optimized regarding operating range and thus strong deviations in pressure losses were not expected. Nevertheless, using this kind of actuation system on highly loaded profiles an influence on pressure losses is probable because smaller operating range of such profiles. Hence, the same actuator performance may have a stronger effect on the aerodynamic performance.

Regarding the aerodynamic experiment quality, there were some penalties in the periodicity of the cascade flow. This had to be accepted because of the manufacturing process which has led to five individual blades with geometry deviations higher than obtained standard blades.

Although, the aim of that technology is to increase off-design performance in terms of operational range and stage efficiency from these results there is no conclusion about efficiency possible. The reason is that the cascade experiment is non-rotating and thus efficiency cannot be calculated. Further investigations in a rotating machinery are intended to quantify that issue.

In general, this experiment shows that piezoceramic actuators together with a blade made of plastics have the ability to manipulate blade shape and thus aerodynamic performance in a cascade experiment. Because of the authors' vision to use this technology for rotating compressor blades, the next planned experiment is on a subsonic rotating test rig. Regarding the experimental setup,

this leads to two major demanding tasks: The first task is to manufacture three-dimensional curved blades. This may lead to a re-design of the presented concept to realize a needed blade twist (For example CFRP as the blade material and actuators with different ceramic orientation). In addition to that, compared to a cascade experiment, much more blades are needed for a test inside a rotating machinery. To keep small geometric deviations resulting from the manufacturing process a new manufacturing technique has to be developed. The second demanding challenge is to transduce the power supply of the actuators into the rotating system of the test rig. Possible solutions are electromagnetic induction or slip rings.

Appendix
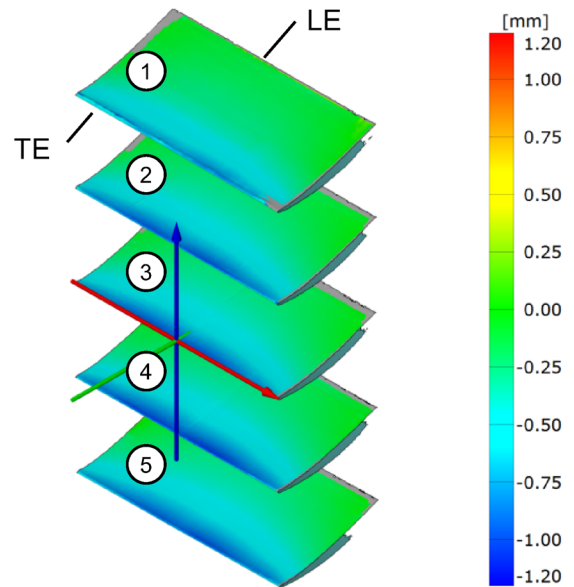
Fig. 22 Blade deformations at the pressure side between condition MAX and REF without aerodynamic loads for $\beta_1 = 25°$
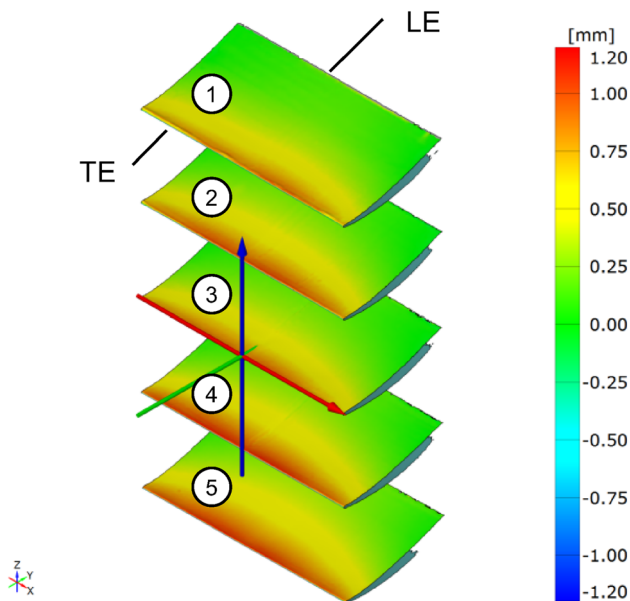
Fig. 21 Blade deformations at the pressure side between condition MIN and REF without aerodynamic loads for $\beta_1 = 25°$
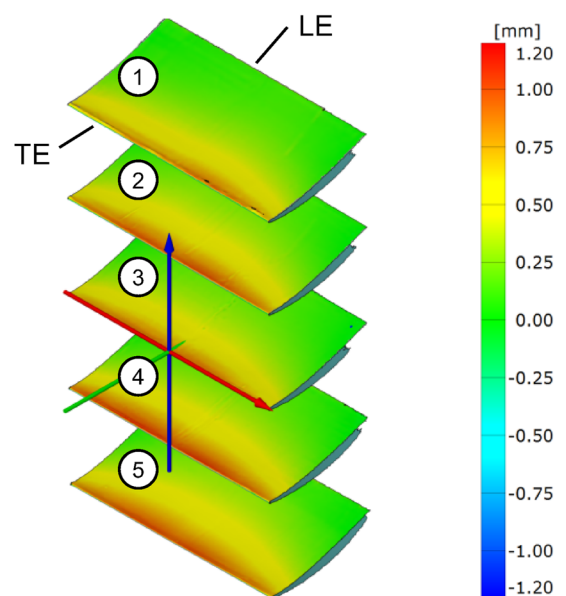
Fig. 23 Blade deformations at the pressure side between condition MIN and REF without aerodynamic loads for $\beta_1 = 45°$
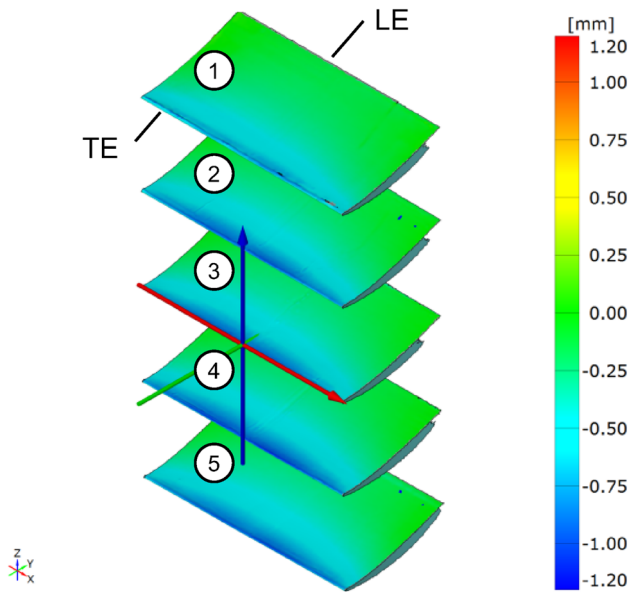
Fig. 24 Blade deformations at the pressure side between condition MAX and REF without aerodynamic loads for $\beta_1 = 45°$
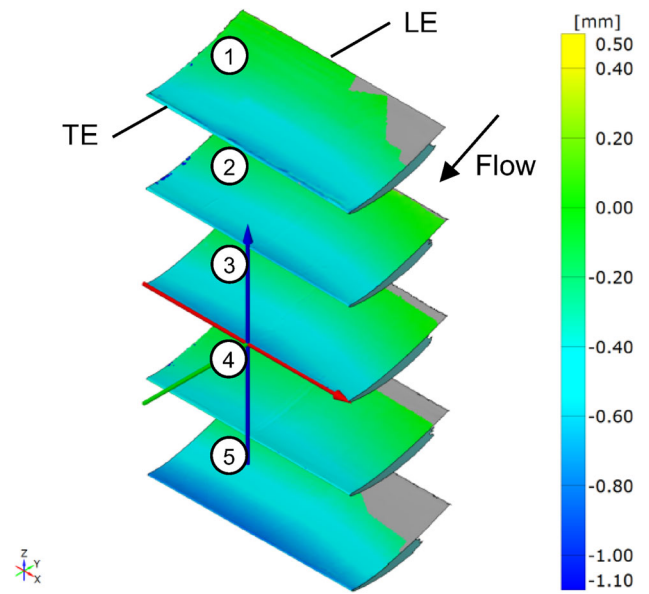
Fig. 26 Blade deformations at the pressure side caused by the flow between condition $\mathrm{MIN_{AL}}$ and MIN for $\beta_1 = 25°$
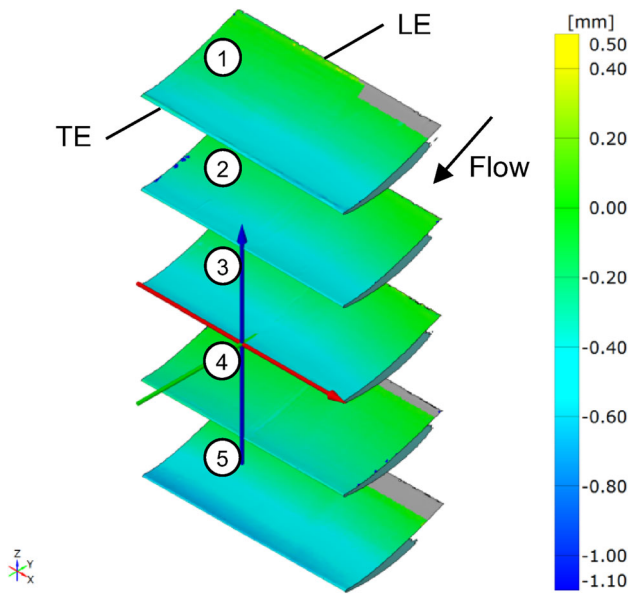
Fig. 25 Blade deformations at the pressure side caused by the flow between condition $\mathrm{REF_{AL}}$ and REF for $\beta_1 = 25°$
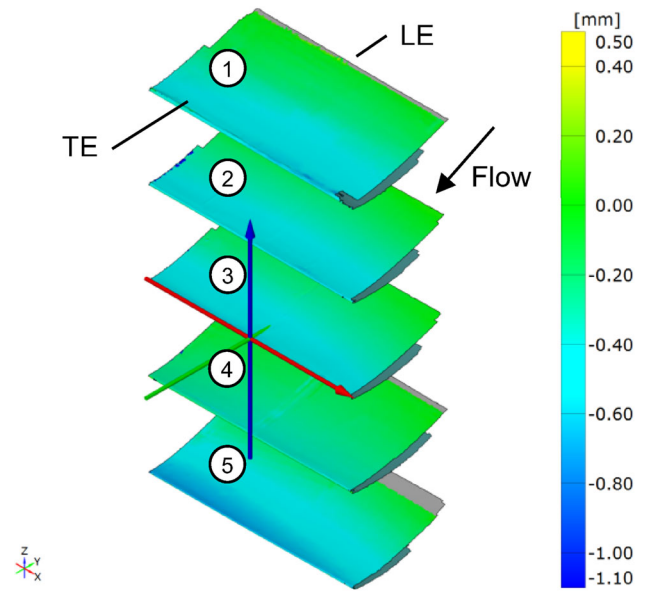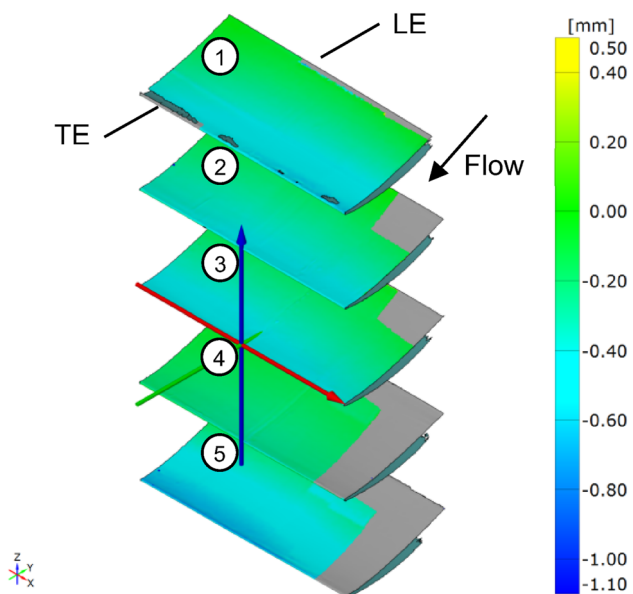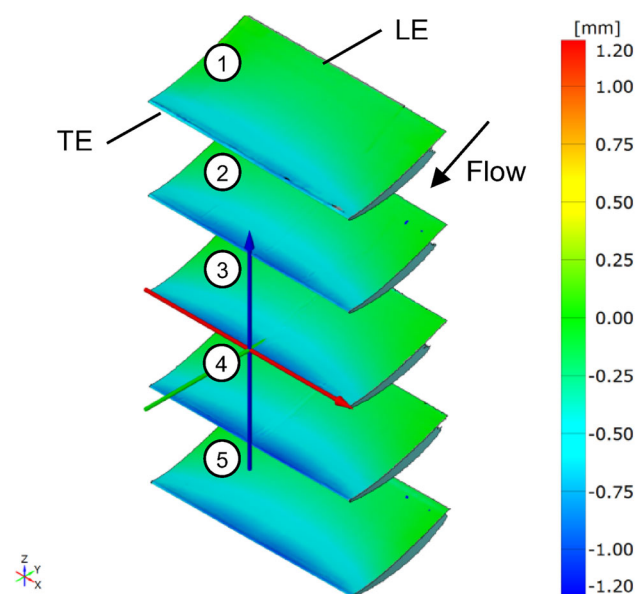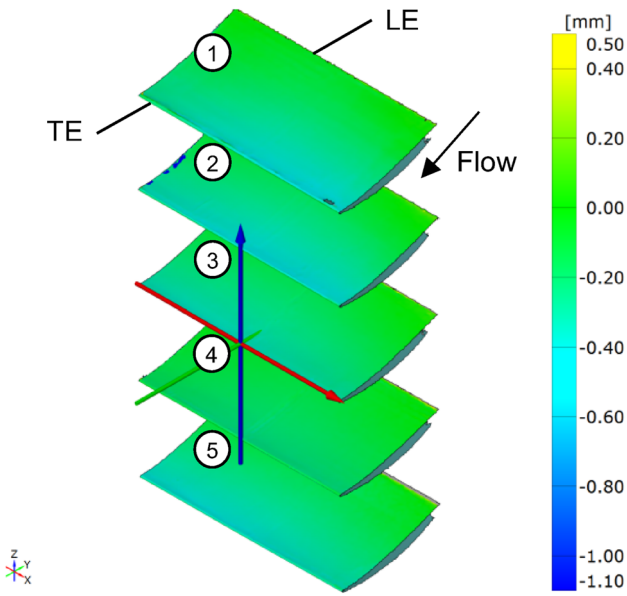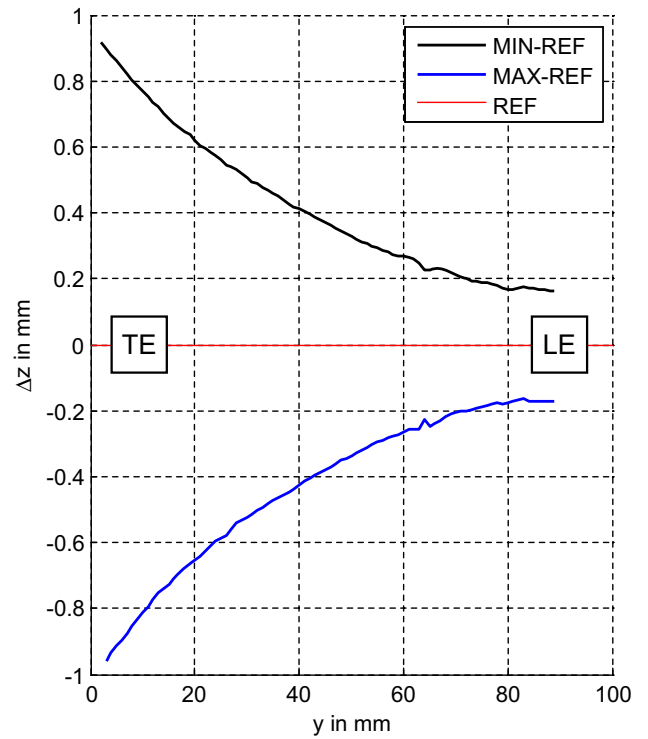

Fig. 27 Blade deformations at the pressure side caused by the flow between condition $\mathrm{MAX_{AL}}$ and MAX for $\beta_1 = 25°$
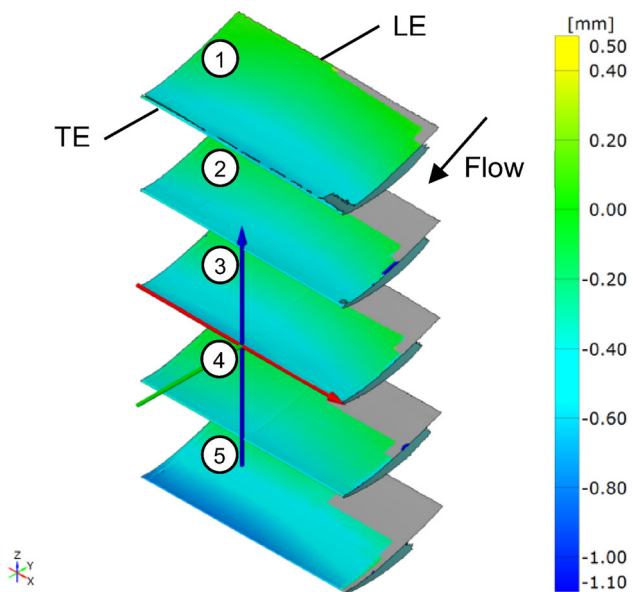
Fig. 28 Blade deformations at the pressure side caused by the flow between condition MIN$_{AL}$ and MIN for $\beta_1 = 30°$
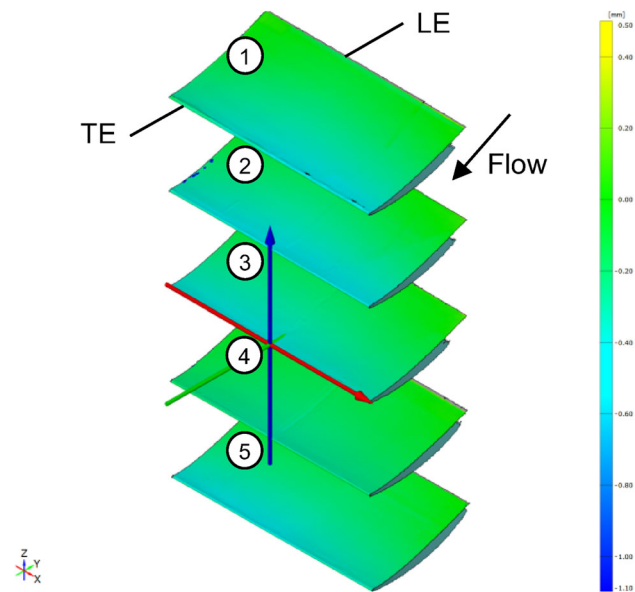
Fig. 30 Blade deformations at the pressure side caused by the flow between condition REF$_{AL}$ and REF for $\beta_1 = 45°$

Fig. 29 Blade deformations at the pressure side caused by the flow between condition MAX$_{AL}$ and MAX for $\beta_1 = 30°$

Fig. 31 Blade deformations at the pressure side caused by the flow between condition MIN$_{AL}$ and MIN for $\beta_1 = 45°$

Fig. 32 Blade deformations at the pressure side caused by the flow between condition MAX_{AL} and MAX for $\beta_1 = 45°$

Fig. 33 Actuator-induced displacements Δz at the middle section of the pressure side of blade 1 for $\beta_1 = 30°$ along chord (y)
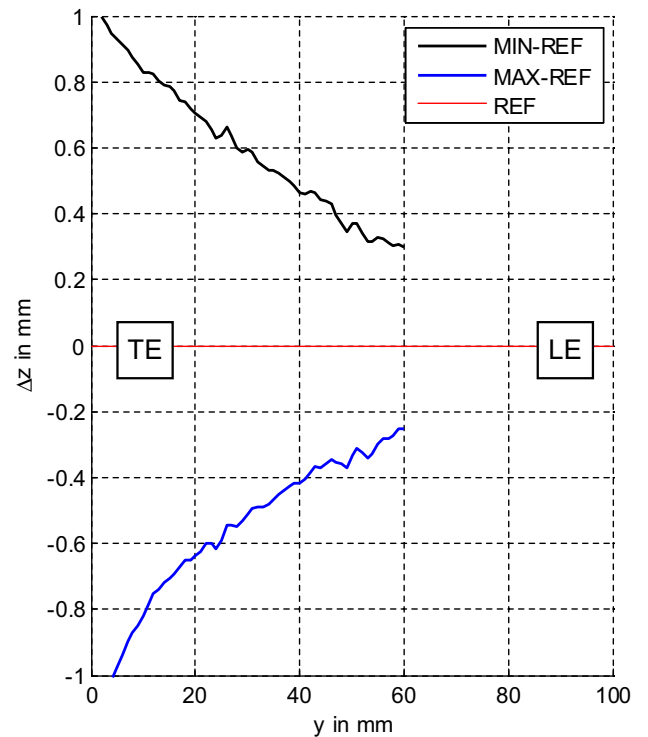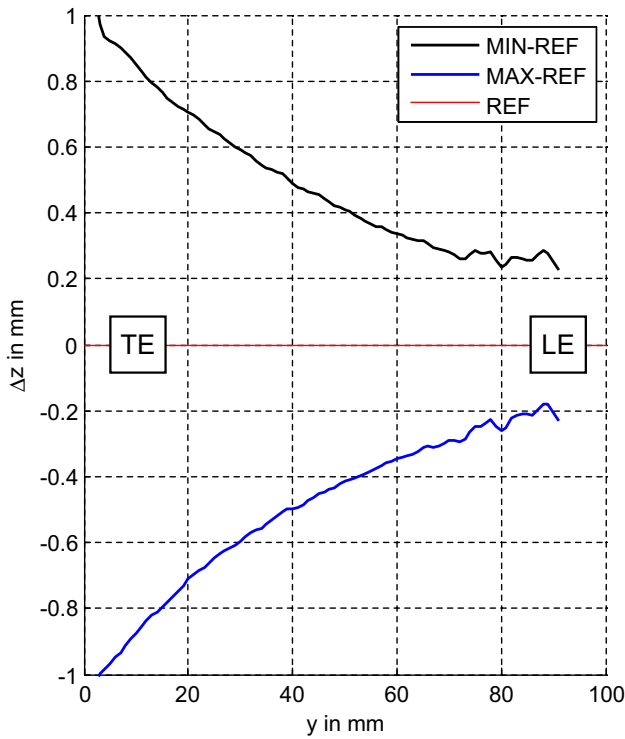

Fig. 34 Actuator-induced displacements Δz at the middle section of the pressure side of blade 2 for $\beta_1 = 30°$ along chord (y)

Fig. 35 Actuator-induced displacements Δz at the middle section of the pressure side of blade 4 for $\beta_1 = 30°$ along chord (y)

Fig. 36 Actuator-induced displacements Δz at the middle section of the pressure side of blade 5 for $\beta_1 = 30°$ along chord (y)
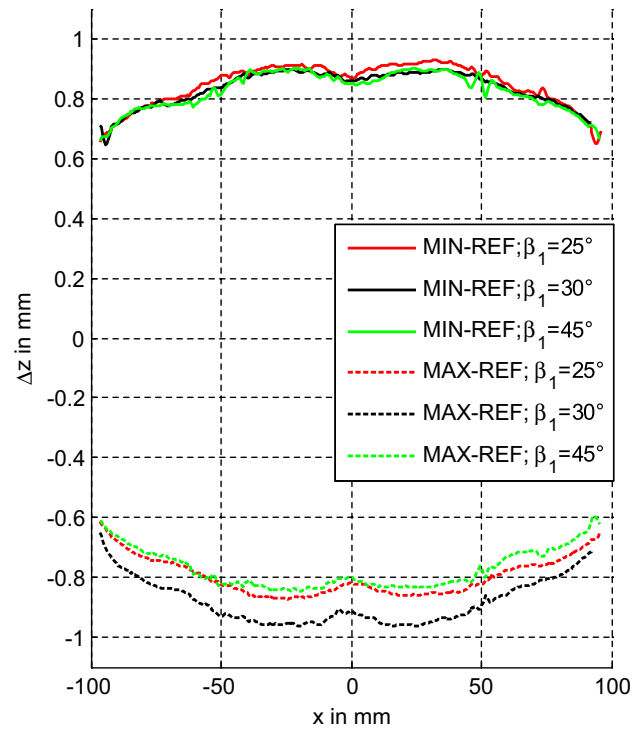

Fig. 38 Actuator-induced trailing edge displacements of blade 2 at $y = 5$ mm for different flow angles over span (x axis) without aerodynamic loads
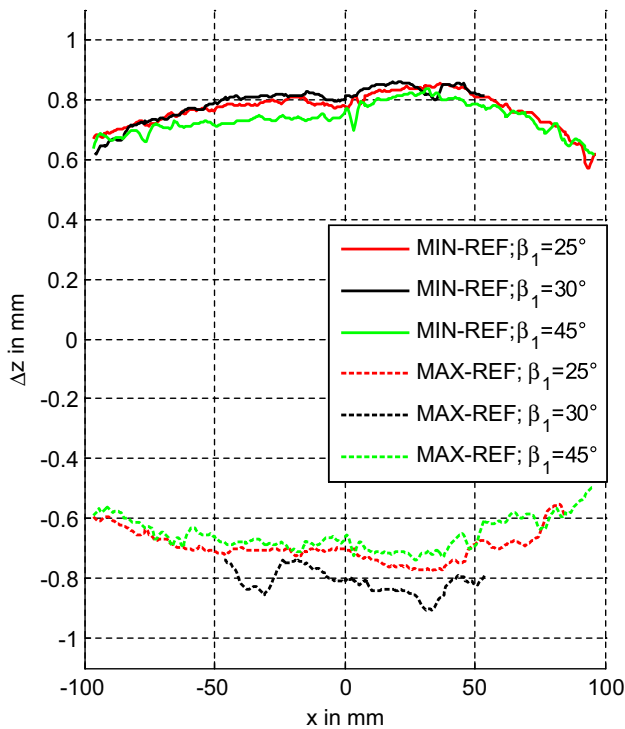

Fig. 37 Actuator-induced trailing edge displacements of blade 1 at $y = 5$ mm for different flow angles over span (x axis) without aerodynamic loads
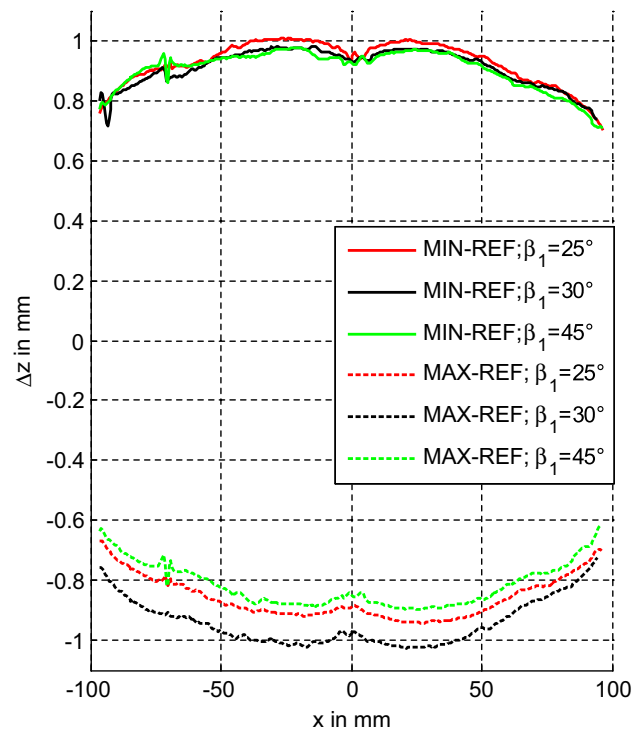

Fig. 39 Actuator-induced trailing edge displacements of blade 4 at $y = 5$ mm for different flow angles over span (x axis) without aerodynamic loads
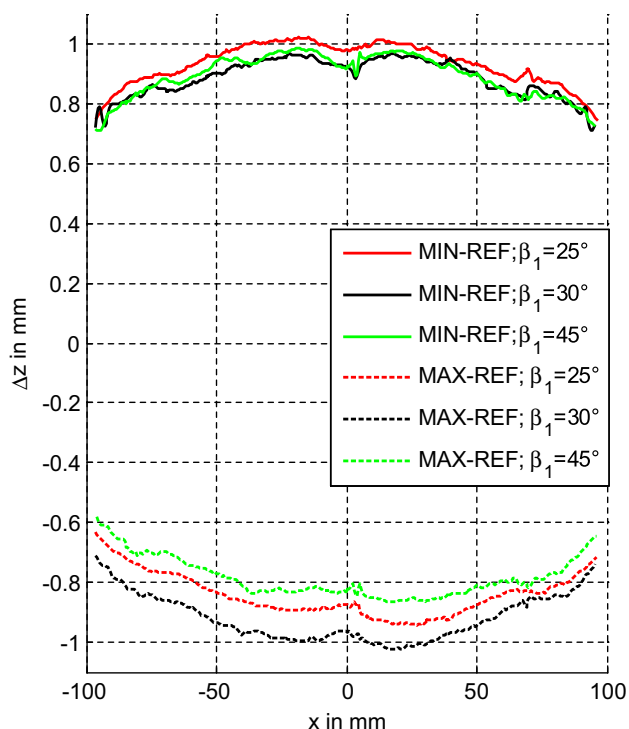
Fig. 40 Actuator-induced trailing edge displacements of blade 5 at $y = 5$ mm for different flow angles over span (x axis) without aerodynamic loads
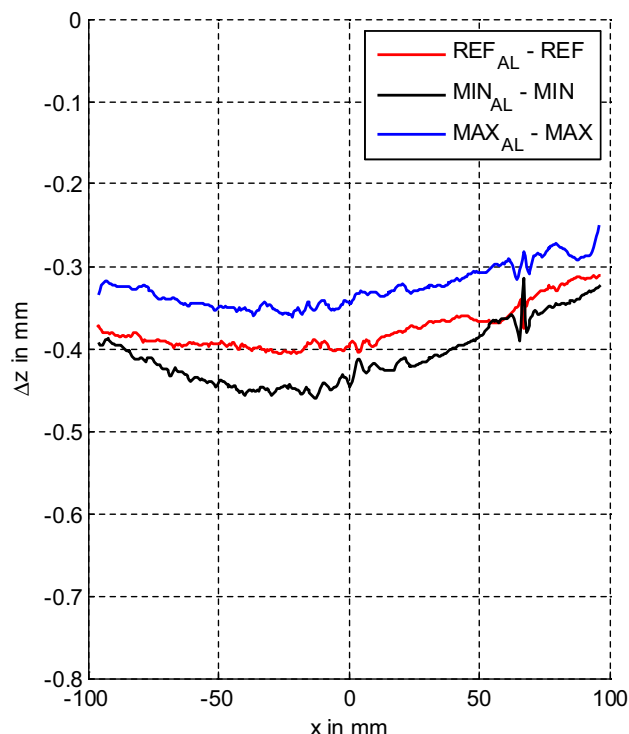

Fig. 42 Trailing edge displacements Δz over span (x axis) of blade 3 at $y = 5$ mm caused by the flow for $\beta_1 = 45°$
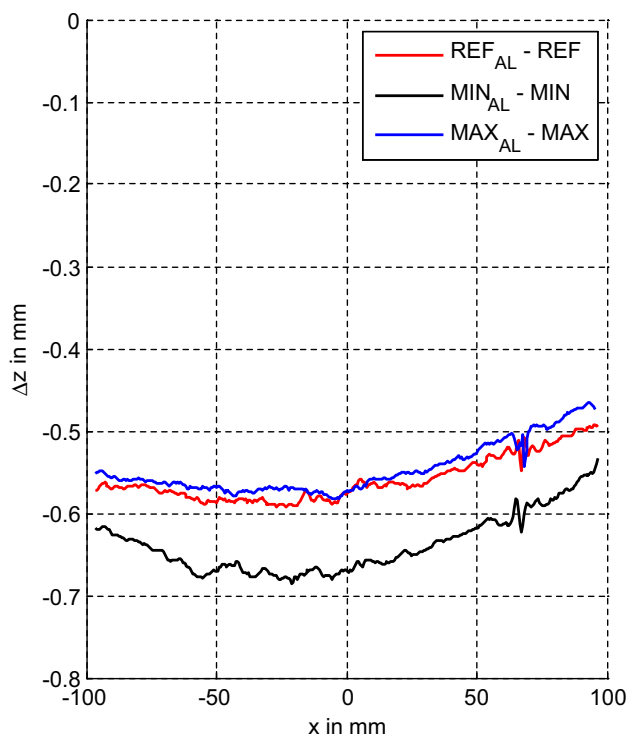
References

1. Rolls-Royce: The Jet engine. s.l. Renault Printing Co Ltd, Schrifttum (1996)
2. Monroe, R.C: Consider variable pitch fans. Houston, Texas. Hudson Products Corp
3. Mazzawy, R. S: Performance study for benefits of variable pitch composite fan. s.l. Proceedings of ASME Turbo Expo 2010 (2010)
4. Forecast International: "Ducted-Prop/Propfan Technologies", Archieved 3/2000 (1999)
5. Violette, J. A., Loss, E. S.: Mechanical design of variable pitch fan for turbofan engines, Proceedings of ASME Turbo Expo 2010, GT2010-22969 (2010)
6. Müller, T., Lawerenz, M.: Shape adaptive airfoils for turbomachinery applications undergoing large deflections, 44th AIAA/ASME/ASCE/AHS Structures, Structural Dynamics and Materials Conference, Norfolk (2003)
7. Müller, T., Dipperz.: Entwicklung und experimentelle Untersuchung einer formvariablen Turbomaschinenschaufel, Fortschritt-Berichte VDI, Vol. 7, Nr. 482, VDI Verlag (2006)
8. Monner, H.P.: Realization of an optimized wing camber by using form variable flap structures. Aerosp. Sci. Technol. **5**(7), 1270–9638 (2001)
9. Hammer et al.: Active flow control by adaptive blade systems in periodic unsteady flow conditions, https://depositonce.tu-berlin.de/bitstream/11303/197/2/HammerPhanPeterWerderMeyerLiebichThamsen2014afcc.pdf
10. Van de Kamp, B.: Konzeptstudie: Strukturkonzept adaptiver Beschaufelungen für Turbofan-Triebwerke, Diploma Thesis, TU Braunschweig (2012)

Fig. 41 Trailing edge displacements Δz over span (x axis) of blade 3 at $y = 5$ mm caused by the flow for $\beta_1 = 25°$

11. Monner, H.P., Huxdorf, O., Riemenschneider, J., Keimer, R.: Design and manufacturing of morphing fan blades for experimental investigations in a cascaded wind tunnel, 23rd AIAA/AHS adaptive structures conference. Kissimmee, Florida (2015)

12. Huxdorf, O.: Auslegung und Bau von Schaufeln mit variabler Wölbung für den Test im Gitterwindkanal, Diploma Thesis, Otto-von-Guericke-University Magdeburg (2013)

13. Riemenschneider, J., Huxdorf, O., Opitz, S.: Effects of piezoceramic actuator in quasistatic use, ASME International Conference on Smart Materials, Adaptive Structures and Intelligent Systems, ASME, Newport, Rhode Island, USA (2014)

14. Schur, F.: Experimentelle Untersuchung einer adaptiven Verdichterbeschaufelung im Gitterwindkanal. Studienarbeit, TU Braunschweig (2015)